†Corresponding email address: sandy.herho@email.ucr.edu

`wave-attenuation-1d`: An idealized one-dimensional framework for wave attenuation through coastal vegetation using Numba-accelerated shallow water equations

Sandy H. S. Herho[1, 2, 3*], Iwan P. Anwar[2, 3], Theo R. E. B. N. Ndruru[2], Rusmawan Suwarman[4], Dasapta E. Irawan[5]

[1*]Department of Earth and Planetary Sciences, University of California, Riverside, 900 University Ave., Riverside, 92521, CA, USA.
[2]Applied and Environmental Oceanography Research Group, Bandung Institute of Technology (ITB), Jalan Ganesha 10, Bandung, 40132, West Java, Indonesia.
[3]Samudera Sains Teknologi (SST) Ltd., Gang Sarimanah XIII/67, Bandung, 40151, West Java, Indonesia.
[4]Atmospheric Science Research Group, Bandung Institute of Technology (ITB), Jalan Ganesha 10, Bandung, 40132, West Java, Indonesia.
[5]Applied Geology Research Group, Bandung Institute of Technology (ITB), Jalan Ganesha 10, Bandung, 40132, West Java, Indonesia.

*Corresponding author(s). E-mail(s): sandy.herho@email.ucr.edu;

Abstract

Coastal vegetation provides crucial wave attenuation for shoreline protection, yet existing models are either computationally prohibitive or lack transparency for educational purposes. This study presents `wave-attenuation-1d`, an open-source Python package implementing linearized shallow water equations with vegetation-induced drag to simulate wave propagation through coastal vegetation. The governing equations are derived from first principles through systematic application of shallow water assumptions, depth-integration, and linearization, yielding coupled continuity and momentum equations where vegetation effects enter as a dissipative drag term proportional to velocity. The numerical implementation employs fourth-order Runge-Kutta time integration with implicit treatment of drag terms on a staggered grid, achieving unconditional stability for stiff dissipative terms. Numerical experiments with monochromatic waves propagating through a 40-meter vegetation patch demonstrate transmission coefficients ranging from 0.799 for sparse vegetation to 0.011 for dense vegetation, corresponding to wave height reductions of 20.1% and 98.9%, respectively. While the one-dimensional framework necessarily simplifies three-dimensional flow structures, turbulence generation, and flexible vegetation dynamics, the model provides a transparent, computationally efficient baseline for understanding fundamental wave-vegetation interactions. The package features standardized NetCDF output with CF-compliant metadata, and modular architecture that facilitates both educational applications and extensions toward more sophisticated models. This work bridges the gap between research-grade simulations and accessible tools for coastal engineering education, providing a foundation for exploring nature-based solutions for coastal protection.

Keywords: Coastal Protection; Coastal Vegetation; Nature-Based Solutions; Numerical Modeling; Shallow Water Equations; Wave Attenuation

MSC Classification: 35Q35; 65M06; 76B15

1 Introduction

Coastal vegetation provides a critical natural defense against wave attack, with field observations demonstrating substantial wave height reductions through marsh systems and significant attenuation through mangrove forests during tropical cyclones [1, 2]. The quantification of wave-vegetation interactions has emerged as a fundamental problem in coastal oceanography, requiring mathematical frameworks that bridge hydrodynamics, plant biomechanics, and turbulence theory. As global coastal populations face increasing storm risk and sea-level rise, understanding and predicting the protective capacity of vegetated shorelines has become essential for sustainable coastal management.

The theoretical foundation for wave attenuation by vegetation traces to Dalrymple et al. [3], who adapted the Morison equation from offshore engineering to model drag forces on rigid cylinders representing plant stems. This pioneering work established the mathematical paradigm still employed in contemporary models: vegetation as a momentum sink acting on the flow field. Subsequent refinements by Kobayashi et al. [4] incorporated probabilistic stem distributions, while Méndez et al. [5] extended the framework to random waves using spectral methods. These early studies demonstrated that linearization of the drag force enabled analytical solutions predicting exponential wave decay through uniform vegetation fields.

Laboratory experiments have revealed fundamental limitations of the rigid-cylinder approximation. Bradley and Houser [6] demonstrated that plant flexibility substantially reduces drag coefficients compared to rigid analogs, with the effective drag depending strongly on the ratio of hydrodynamic to elastic restoring forces. The three-dimensional flow structure around vegetation, characterized by horseshoe vortices, von Kármán vortex streets, and turbulent wakes, generates momentum transport mechanisms absent from depth-averaged formulations [7]. Recent direct numerical simulations by Chalmoukis et al. [8] have captured these multiscale interactions, revealing that turbulence production accounts for a significant portion of total energy dissipation—a process fundamentally inaccessible to one-dimensional models.

Contemporary studies have advanced along three complementary directions. First, the incorporation of flexible vegetation dynamics through coupled fluid-structure interaction models, exemplified by the immersed boundary methods [9] and the modal decomposition approaches [10]. These studies show that plant reconfiguration under wave loading follows predictable patterns that significantly modify the effective drag. Second, the extension to spectral wave environments, where frequency-dependent attenuation modifies the wave spectrum [11–13]. Field observations confirm that high-frequency components attenuate preferentially, leading to period lengthening and spectral narrowing. Third, the integration of vegetation models into phase-resolving codes such as SWASH [14], Boussinesq-type models [15, 16], and smoothed particle hydrodynamics frameworks [17]. These advances have enabled simulations approaching field-scale complexity, yet fundamental questions persist regarding the appropriate level of physical detail for engineering applications.

Despite these advances, a significant gap exists between sophisticated research models and practical tools accessible to coastal engineers and students. High-fidelity simulations remain computationally prohibitive for routine design calculations, while commercial software often implements vegetation effects through opaque parameterizations. Furthermore, the proliferation of modeling approaches has made it difficult to establish benchmark solutions and compare methodologies. The coastal engineering community requires transparent, well-documented implementations that facilitate understanding of the underlying physics while acknowledging inherent limitations.

The principles of open science have become increasingly vital in science and engineering studies [18, 19], particularly as communities worldwide seek sustainable solutions for coastal protection [20, 21]. Open-source software development enables scientists and engineers from diverse geographical and economic backgrounds to access, validate, and contribute to scientific tools, democratizing the research process [22]. This is especially critical for coastal vegetation modeling, where local knowledge and field observations from various ecosystems can inform model improvements. By making our code freely available and well-documented, we enable scientists and engineers in developing nations—often those most vulnerable to coastal hazards—to adapt and apply these tools to their specific contexts. Furthermore, open science practices enhance reproducibility, a cornerstone of scientific integrity that has gained renewed emphasis in computational sciences. The ability to scrutinize, modify, and extend numerical models fosters collaborative improvement and helps identify limitations that might remain hidden in proprietary implementations.

The choice of Python as the development language reflects its emergence as the lingua franca of scientific computing and engineering analysis. Python's extensive ecosystem, including NumPy for numerical operations [23], SciPy for scientific algorithms [24], and specialized libraries for oceanographic applications, has transformed how scientists and engineers approach computational problems [25]. The language's emphasis on readability and rapid prototyping enables scientists to focus on physical understanding rather than implementation details [26, 27]. Moreover, the availability of just-in-time compilation tools like Numba has addressed Python's traditional performance limitations, enabling execution speeds approaching compiled languages while maintaining development flexibility [28]. This combination of accessibility, performance, and community support makes Python particularly suitable for creating educational tools that can also serve research purposes. The language's gentle learning curve particularly benefits students and researchers transitioning from other disciplines, fostering interdisciplinary collaboration essential for addressing complex coastal challenges.

The present work addresses this gap by providing an open-source Python implementation of wave attenuation through vegetation using linearized shallow water equations. Our package, accelerated through just-in-time compilation, achieves computational efficiency suitable for parameter studies while maintaining code transparency essential for educational purposes. We explicitly position this as a pedagogical tool and baseline for more sophisticated approaches rather than a predictive model for field conditions. The comprehensive documentation of assumptions, numerical methods, and limitations facilitates appropriate use and extension by the research community. By leveraging Python's scientific computing capabilities and adhering to modern software development practices, including version control, automated testing, and comprehensive documentation, we aim to bridge the divide between theoretical understanding and practical application in coastal vegetation modeling. The package's distribution through standard channels (PyPI) and the provision of all data and analysis scripts ensures that our results can be independently verified and built upon, embodying the open science ethos that accelerates scientific progress in addressing coastal resilience challenges.

2 Methods

2.1 Mathematical Formulation

The wave attenuation model requires derivation from first principles to establish the governing equations for wave propagation through coastal vegetation. The derivation proceeds from the three-dimensional Navier-Stokes equations through application of shallow water assumptions, depth integration, and linearization.

The motion of an incompressible, viscous fluid obeys the conservation of mass and momentum. In an Eulerian framework [29, 30], the three-dimensional Navier-Stokes equations in Cartesian coordinates (x, y, z) with velocity components $\mathbf{u} \equiv (u, v, w)$ are:

$$\nabla \cdot \mathbf{u} \equiv \frac{\partial u}{\partial x} + \frac{\partial v}{\partial y} + \frac{\partial w}{\partial z} = 0, \tag{1}$$

$$\rho \frac{D\mathbf{u}}{Dt} = -\nabla p + \mu \nabla^2 \mathbf{u} + \rho \mathbf{f}, \tag{2}$$

where $D/Dt \equiv \partial/\partial t + \mathbf{u} \cdot \nabla$ denotes the material derivative, ρ is the fluid density (constant for incompressible flow), p is the pressure field, μ is the dynamic viscosity, and $\mathbf{f}$ represents body forces per unit mass.

Expanding equation (2) in component form with $\mathbf{f} = (f_x, f_y, f_z - g)$ where g is gravitational acceleration:

$$\begin{aligned}
\frac{\partial u}{\partial t} + u\frac{\partial u}{\partial x} + v\frac{\partial u}{\partial y} + w\frac{\partial u}{\partial z} &= -\frac{1}{\rho}\frac{\partial p}{\partial x} + \nu\left(\frac{\partial^2 u}{\partial x^2} + \frac{\partial^2 u}{\partial y^2} + \frac{\partial^2 u}{\partial z^2}\right) + f_x, \\
\frac{\partial v}{\partial t} + u\frac{\partial v}{\partial x} + v\frac{\partial v}{\partial y} + w\frac{\partial v}{\partial z} &= -\frac{1}{\rho}\frac{\partial p}{\partial y} + \nu\left(\frac{\partial^2 v}{\partial x^2} + \frac{\partial^2 v}{\partial y^2} + \frac{\partial^2 v}{\partial z^2}\right) + f_y, \\
\frac{\partial w}{\partial t} + u\frac{\partial w}{\partial x} + v\frac{\partial w}{\partial y} + w\frac{\partial w}{\partial z} &= -\frac{1}{\rho}\frac{\partial p}{\partial z} + \nu\left(\frac{\partial^2 w}{\partial x^2} + \frac{\partial^2 w}{\partial y^2} + \frac{\partial^2 w}{\partial z^2}\right) - g + f_z,
\end{aligned} \tag{3}$$

where $\nu \equiv \mu/\rho$ is the kinematic viscosity.

To derive the shallow water equations, scale analysis determines the relative importance of each term. Following Stoker [31] and Peregrine [32], introduce characteristic scales:

$$\begin{aligned}
&\text{Horizontal length:} \quad L \\
&\text{Vertical length:} \quad h_0 \\
&\text{Horizontal velocity:} \quad U \\
&\text{Vertical velocity:} \quad W \\
&\text{Time:} \quad T \equiv L/U \\
&\text{Pressure:} \quad P \equiv \rho g h_0
\end{aligned} \tag{4}$$

The dimensionless variables become:

$$\begin{aligned}
(x^*, y^*) &\equiv (x/L, y/L), \quad z^* \equiv z/h_0, \quad t^* \equiv t/T, \\
(u^*, v^*) &\equiv (u/U, v/U), \quad w^* \equiv w/W, \quad p^* \equiv p/P.
\end{aligned} \tag{5}$$

The aspect ratio $\epsilon \equiv h_0/L$ characterizes the flow geometry. For shallow water, $\epsilon \ll 1$. From the continuity equation (1), dimensional analysis yields:

$$\frac{U}{L} + \frac{U}{L} + \frac{W}{h_0} = 0, \tag{6}$$

which requires $W = O(\epsilon U)$ for consistency.

Substituting the scalings into the vertical momentum equation:

$$\frac{\epsilon U^2}{L}\frac{\partial w^*}{\partial t^*} + \frac{\epsilon U^2}{L}\left(u^*\frac{\partial w^*}{\partial x^*} + v^*\frac{\partial w^*}{\partial y^*} + w^*\frac{\partial w^*}{\partial z^*}\right) = -\frac{g}{\epsilon}\frac{\partial p^*}{\partial z^*} + \frac{\nu\epsilon U}{h_0^2}\nabla^{*2}w^* - g. \tag{7}$$

Multiplying by ϵ/g and taking the limit $\epsilon \to 0$:

$$0 = -\frac{\partial p^*}{\partial z^*} - 1 + O(\epsilon^2). \tag{8}$$

In dimensional form, this yields the hydrostatic approximation:

$$\frac{\partial p}{\partial z} = -\rho g. \tag{9}$$

The physical interpretation is that vertical accelerations are negligible compared to gravitational forces when horizontal scales greatly exceed vertical scales. This approximation breaks down near sharp bottom features where $\partial h/\partial x = O(1)$ rather than $O(\epsilon)$.

Integration of equation (9) from depth z to the free surface $z = \eta(x, y, t)$ where pressure equals atmospheric pressure p_a:

$$p(x, y, z, t) = p_a + \int_z^\eta \rho g \, dz' = p_a + \rho g[\eta(x, y, t) - z]. \tag{10}$$

The horizontal pressure gradients become:

$$\nabla_h p \equiv \left(\frac{\partial p}{\partial x}, \frac{\partial p}{\partial y}\right) = \rho g \nabla_h \eta, \tag{11}$$

where ∇_h denotes the horizontal gradient operator.

Depth integration transforms the three-dimensional equations into two-dimensional form. Define the total water depth:

$$H(x, y, t) \equiv h(x, y) + \eta(x, y, t), \tag{12}$$

where $h(x, y)$ is the still water depth and $\eta(x, y, t)$ is the free surface elevation above mean water level.

The depth-averaged velocities are:

$$\begin{aligned} \bar{u}(x, y, t) &\equiv \frac{1}{H} \int_{-h}^{\eta} u(x, y, z, t) \, dz, \\ \bar{v}(x, y, t) &\equiv \frac{1}{H} \int_{-h}^{\eta} v(x, y, z, t) \, dz. \end{aligned} \tag{13}$$

The kinematic boundary conditions express the impermeability of boundaries. At the free surface $z = \eta(x, y, t)$:

$$\frac{D}{Dt}[z - \eta(x, y, t)] = 0, \tag{14}$$

which expands to:

$$w = \frac{\partial \eta}{\partial t} + u\frac{\partial \eta}{\partial x} + v\frac{\partial \eta}{\partial y} \quad \text{at} \quad z = \eta. \tag{15}$$

At the rigid bottom $z = -h(x, y)$:

$$w = -u\frac{\partial h}{\partial x} - v\frac{\partial h}{\partial y} \quad \text{at} \quad z = -h. \tag{16}$$

To integrate the continuity equation, apply Leibniz's integral rule. For a general function $f(x, y, z, t)$ with moving boundaries:

$$\frac{\partial}{\partial x}\int_{a(x)}^{b(x)} f(x,z)\,dz = \int_{a(x)}^{b(x)} \frac{\partial f}{\partial x}\,dz + f\big|_{z=b(x)}\frac{\partial b}{\partial x} - f\big|_{z=a(x)}\frac{\partial a}{\partial x}. \tag{17}$$

Applying this to integrate equation (1):

$$\begin{aligned} 0 &= \int_{-h}^{\eta}\left(\frac{\partial u}{\partial x} + \frac{\partial v}{\partial y} + \frac{\partial w}{\partial z}\right) dz \\ &= \frac{\partial}{\partial x}\int_{-h}^{\eta} u\,dz - u\big|_{z=\eta}\frac{\partial \eta}{\partial x} + u\big|_{z=-h}\frac{\partial h}{\partial x} \\ &\quad + \frac{\partial}{\partial y}\int_{-h}^{\eta} v\,dz - v\big|_{z=\eta}\frac{\partial \eta}{\partial y} + v\big|_{z=-h}\frac{\partial h}{\partial y} \\ &\quad + w\big|_{z=\eta} - w\big|_{z=-h}. \end{aligned} \tag{18}$$

Substituting the boundary conditions (15) and (16):

$$\frac{\partial H}{\partial t} + \frac{\partial}{\partial x}(H\bar{u}) + \frac{\partial}{\partial y}(H\bar{v}) = 0. \tag{19}$$

The momentum equations require similar treatment. Integrating the x-momentum equation and using the hydrostatic pressure distribution:

$$\begin{aligned} &\int_{-h}^{\eta}\frac{\partial u}{\partial t}\,dz + \int_{-h}^{\eta}\left(u\frac{\partial u}{\partial x} + v\frac{\partial u}{\partial y} + w\frac{\partial u}{\partial z}\right) dz \\ &= -\frac{g}{\rho}\int_{-h}^{\eta}\rho\frac{\partial \eta}{\partial x}\,dz + \int_{-h}^{\eta}\left(\nu\nabla^2 u + f_x\right) dz. \end{aligned} \tag{20}$$

The pressure term simplifies to:

$$-\frac{g}{\rho}\int_{-h}^{\eta}\rho\frac{\partial \eta}{\partial x}\,dz = -gH\frac{\partial \eta}{\partial x}. \tag{21}$$

The nonlinear advection terms require the introduction of dispersion corrections for non-uniform velocity profiles [33]. However, for long waves where $kh \ll 1$ (with k being the wavenumber), the velocity profile is nearly uniform and these corrections are small.

After integration and algebraic manipulation, the two-dimensional shallow water equations become:

$$\begin{aligned}
\frac{\partial H}{\partial t} + \frac{\partial (H\bar{u})}{\partial x} + \frac{\partial (H\bar{v})}{\partial y} &= 0, \\
\frac{\partial (H\bar{u})}{\partial t} + \frac{\partial}{\partial x}\left(H\bar{u}^2 + \frac{gH^2}{2}\right) + \frac{\partial (H\bar{u}\bar{v})}{\partial y} &= -gH\frac{\partial h}{\partial x} + F_x, \\
\frac{\partial (H\bar{v})}{\partial t} + \frac{\partial (H\bar{u}\bar{v})}{\partial x} + \frac{\partial}{\partial y}\left(H\bar{v}^2 + \frac{gH^2}{2}\right) &= -gH\frac{\partial h}{\partial y} + F_y,
\end{aligned} \tag{22}$$

where F_x and F_y represent depth-integrated external forces including bottom friction and vegetation drag.

For one-dimensional propagation in a prismatic channel of constant depth h, the equations reduce to:

$$\begin{aligned}
\frac{\partial \eta}{\partial t} + \frac{\partial}{\partial x}[(h+\eta)u] &= 0, \\
\frac{\partial u}{\partial t} + u\frac{\partial u}{\partial x} + g\frac{\partial \eta}{\partial x} &= \frac{F_x}{h+\eta},
\end{aligned} \tag{23}$$

where the overbar notation has been dropped.

Linearization assumes small perturbations from the quiescent state. Let:

$$\eta = \varepsilon\eta', \quad u = \varepsilon u', \tag{24}$$

where $\varepsilon \ll 1$ measures the wave amplitude relative to depth, and primed variables are $O(1)$. Substituting into (23):

$$\begin{aligned}
\varepsilon\frac{\partial \eta'}{\partial t} + \frac{\partial}{\partial x}[(h+\varepsilon\eta')\varepsilon u'] &= 0, \\
\varepsilon\frac{\partial u'}{\partial t} + \varepsilon^2 u'\frac{\partial u'}{\partial x} + g\varepsilon\frac{\partial \eta'}{\partial x} &= \frac{F_x}{h+\varepsilon\eta'}.
\end{aligned} \tag{25}$$

Expanding $(h+\varepsilon\eta')^{-1} = h^{-1}[1-\varepsilon\eta'/h + O(\varepsilon^2)]$ and retaining only $O(\varepsilon)$ terms:

$$\begin{aligned}
\frac{\partial \eta'}{\partial t} + h\frac{\partial u'}{\partial x} &= 0, \\
\frac{\partial u'}{\partial t} + g\frac{\partial \eta'}{\partial x} &= \frac{F_x}{h}.
\end{aligned} \tag{26}$$

Dropping primes for notational simplicity yields the linearized equations.

Vegetation effects enter through the drag force. Following Dalrymple et al. [3], the drag force per unit volume on a cylindrical stem is:

$$f_D = \frac{1}{2}\rho C_D D|u|u, \tag{27}$$

where C_D is the drag coefficient and D is the cylinder diameter. For N stems per unit horizontal area with height h_v, the depth-integrated force becomes:

$$F_x = -\int_0^{h_v} N f_D \, dz = -\frac{1}{2}\rho C_D N D h_v |u| u. \tag{28}$$

Recent experiments [7, 34] validated this formulation for both emergent ($h_v > h$) and submerged ($h_v < h$) vegetation.

For oscillatory flow with amplitude u_0 and frequency ω, the time-averaged drag force is:

$$\langle F_x \rangle = -\frac{1}{T}\int_0^T \frac{1}{2}\rho C_D N D h_v |u_0 \sin(\omega t)| u_0 \sin(\omega t) \, dt = -\frac{4}{3\pi}\rho C_D N D h_v u_0^2. \tag{29}$$

Linearization assumes $|u|u \approx \bar{u}u$ where $\bar{u} = (8/3\pi)u_0$ is an equivalent steady velocity [4]. The linearized drag coefficient becomes:

$$c_D \equiv \frac{4}{3\pi h} C_D N D h_v u_0. \tag{30}$$

Introducing the vegetation indicator function:

$$\chi_{\text{veg}}(x) \equiv \begin{cases} 1 & \text{if } x \in \text{vegetation zone}, \\ 0 & \text{otherwise}, \end{cases} \tag{31}$$

the final linearized shallow water equations with vegetation become:

$$\begin{aligned} \frac{\partial \eta}{\partial t} + h\frac{\partial u}{\partial x} &= 0, \\ \frac{\partial u}{\partial t} + g\frac{\partial \eta}{\partial x} &= -c_D \chi_{\text{veg}}(x) u. \end{aligned} \tag{32}$$

These equations describe the propagation and attenuation of small-amplitude waves through regions of coastal vegetation, forming the mathematical basis for the numerical model.

2.2 Numerical Implementation

The linearized shallow water equations with vegetation drag given by (32) require careful numerical treatment to accurately capture wave propagation while maintaining stability in the presence of dissipative terms. We develop a semi-discrete formulation using method of lines, where spatial discretization is performed first, followed by temporal integration.

Consider the computational domain $\Omega = [0, L]$ discretized into N_x cells of uniform width $\Delta x = L/N_x$. Following LeVeque [35], we employ a staggered grid arrangement where the free surface elevation η is defined at cell centers:

$$x_i = i\Delta x, \quad i = 0, 1, \ldots, N_x, \tag{33}$$

while the velocity u is defined at cell interfaces:

$$x_{i-1/2} = \left(i - \frac{1}{2}\right)\Delta x, \quad i = 1, 2, \ldots, N_x. \tag{34}$$

This staggering preserves the natural coupling between η and u in the continuous equations and avoids spurious pressure-velocity decoupling.

The semi-discrete approximation of equation (32) becomes:

$$\frac{d\eta_i}{dt} = -\frac{h}{\Delta x}(u_{i+1/2} - u_{i-1/2}), \quad i = 1, 2, \ldots, N_x - 1, \tag{35}$$

$$\frac{du_{i-1/2}}{dt} = -\frac{g}{\Delta x}(\eta_i - \eta_{i-1}) - c_D \chi_{\text{veg}}(x_{i-1/2}) u_{i-1/2}, \quad i = 1, 2, \ldots, N_x. \tag{36}$$

The discrete vegetation indicator function is defined as:

$$\chi_{\text{veg}}(x_{i-1/2}) = \begin{cases} 1 & \text{if } x_{i-1/2} \in [x_{\text{veg,start}}, x_{\text{veg,end}}], \\ 0 & \text{otherwise.} \end{cases} \tag{37}$$

To analyze the spatial discretization error, we expand the continuous variables in Taylor series. For the velocity divergence term:

$$\begin{aligned} \left.\frac{\partial u}{\partial x}\right|_{x_i} &= \frac{u(x_i + \Delta x/2) - u(x_i - \Delta x/2)}{\Delta x} + O(\Delta x^2) \\ &= \frac{u_{i+1/2} - u_{i-1/2}}{\Delta x} + O(\Delta x^2), \end{aligned} \tag{38}$$

confirming second-order spatial accuracy. Similarly, for the pressure gradient:

$$\left.\frac{\partial \eta}{\partial x}\right|_{x_{i-1/2}} = \frac{\eta_i - \eta_{i-1}}{\Delta x} + O(\Delta x^2). \tag{39}$$

The semi-discrete system (35)–(36) can be written in vector form as:

$$\frac{d\boldsymbol{\psi}}{dt} = \mathbf{L}\boldsymbol{\psi} + \mathbf{N}(\boldsymbol{\psi}), \tag{40}$$

where $\boldsymbol{\psi} = [\eta_1, \ldots, \eta_{N_x-1}, u_{1/2}, \ldots, u_{N_x-1/2}]^T$ is the state vector, $\mathbf{L}$ is the linear operator containing spatial derivatives and drag terms, and $\mathbf{N}$ represents nonlinear boundary conditions.

For time integration, we employ the classical fourth-order Runge-Kutta method. However, the presence of the drag term $c_D u$ introduces stiffness when $c_D \Delta t \gg 1$.

Following Ascher et al. [36], we adopt an implicit-explicit (IMEX) approach where the stiff drag term is integrated analytically within each RK4 stage.

Consider a single RK4 stage for the velocity equation:

$$\frac{du^*_{i-1/2}}{dt} = -\frac{g}{\Delta x}(\eta_i - \eta_{i-1}) - c_D \chi_{i-1/2} u^*_{i-1/2}, \tag{41}$$

where the asterisk denotes an intermediate stage value. This can be rewritten as:

$$\frac{du^*_{i-1/2}}{dt} + c_D \chi_{i-1/2} u^*_{i-1/2} = F_{i-1/2}, \tag{42}$$

where $F_{i-1/2} = -g(\eta_i - \eta_{i-1})/\Delta x$ is the pressure gradient forcing. The analytical solution over a time interval τ is:

$$u^*_{i-1/2}(\tau) = u^*_{i-1/2}(0)e^{-c_D\chi_{i-1/2}\tau} + \frac{F_{i-1/2}}{c_D\chi_{i-1/2}}\left(1 - e^{-c_D\chi_{i-1/2}\tau}\right). \tag{43}$$

For regions without vegetation ($\chi_{i-1/2} = 0$), equation (43) reduces to:

$$u^*_{i-1/2}(\tau) = u^*_{i-1/2}(0) + F_{i-1/2}\tau, \tag{44}$$

recovering the standard explicit update.

The complete RK4 algorithm with implicit drag treatment proceeds as follows. Define the operator $\mathcal{F}$ that evaluates the right-hand side of the semi-discrete equations:

$$\mathcal{F}(\boldsymbol{\psi}) = \begin{bmatrix} -h\mathbf{D}_x\mathbf{u} \\ -g\mathbf{G}_x\boldsymbol{\eta} \end{bmatrix}, \tag{45}$$

where $\mathbf{D}_x$ and $\mathbf{G}_x$ are the discrete divergence and gradient operators, respectively.

The four RK4 stages are computed as:

$$\begin{aligned} \mathbf{k}_1 &= \Delta t \cdot \mathcal{F}(\boldsymbol{\psi}^n), \\ \boldsymbol{\psi}_1 &= \mathcal{S}(\Delta t/2)\left[\boldsymbol{\psi}^n + \mathbf{k}_1/2\right], \\ \mathbf{k}_2 &= \Delta t \cdot \mathcal{F}(\boldsymbol{\psi}_1), \\ \boldsymbol{\psi}_2 &= \mathcal{S}(\Delta t/2)\left[\boldsymbol{\psi}^n + \mathbf{k}_2/2\right], \\ \mathbf{k}_3 &= \Delta t \cdot \mathcal{F}(\boldsymbol{\psi}_2), \\ \boldsymbol{\psi}_3 &= \mathcal{S}(\Delta t)\left[\boldsymbol{\psi}^n + \mathbf{k}_3\right], \\ \mathbf{k}_4 &= \Delta t \cdot \mathcal{F}(\boldsymbol{\psi}_3), \end{aligned} \tag{46}$$

where $\mathcal{S}(\tau)$ is the solution operator for the drag term over time τ:

$$[\mathcal{S}(\tau)\mathbf{v}]_{i-1/2} = v_{i-1/2} \cdot \begin{cases} (1 + c_D\tau)^{-1} & \text{if } \chi_{i-1/2} = 1, \\ 1 & \text{if } \chi_{i-1/2} = 0, \end{cases} \tag{47}$$

for the velocity components. The final update is:

$$\boldsymbol{\psi}^{n+1} = \boldsymbol{\psi}^n + \frac{1}{6}(\mathbf{k}_1 + 2\mathbf{k}_2 + 2\mathbf{k}_3 + \mathbf{k}_4). \tag{48}$$

Stability analysis of the numerical scheme requires examining the eigenvalues of the discrete operator. For the linearized system without drag, von Neumann analysis yields the dispersion relation:

$$\omega_{\text{num}}^2 = \frac{4gh}{\Delta x^2}\sin^2\left(\frac{k\Delta x}{2}\right), \tag{49}$$

where k is the wavenumber. The numerical phase speed is:

$$c_{\text{num}} = \frac{\omega_{\text{num}}}{k} = c_0\frac{\sin(k\Delta x/2)}{k\Delta x/2}, \tag{50}$$

showing that $c_{\text{num}} < c_0$ (numerical dispersion) with relative error $O((k\Delta x)^2)$ for well-resolved waves.

The CFL condition for the explicit RK4 scheme is derived from the stability region of the method. For the advection equation $\partial u/\partial t + c\partial u/\partial x = 0$, the amplification factor must satisfy $|G| \leq 1$, yielding:

$$\Delta t \leq \frac{2.8}{\lambda_{\max}} = \frac{2.8\Delta x}{c_0}, \tag{51}$$

where $\lambda_{\max} = c_0/\Delta x$ is the maximum eigenvalue magnitude. In practice, a more conservative CFL number of 0.4 is used:

$$\Delta t = \text{CFL}\cdot\frac{\Delta x}{c_0}, \quad \text{CFL} = 0.4. \tag{52}$$

Boundary conditions require special treatment to maintain accuracy and stability. At the wave generation boundary ($x = 0$), we impose:

$$\eta_0^n = A\sin(\omega t^n), \quad u_{1/2}^n = \sqrt{\frac{g}{h}}\eta_0^n, \tag{53}$$

where the velocity condition follows from the characteristic relation $u = \sqrt{g/h}\eta$ for rightward-propagating shallow water waves.

At the radiation boundary ($x = L$), the Sommerfeld condition [37] is discretized using characteristics. For a quantity ϕ satisfying the advection equation with speed c_0, the discrete update is:

$$\phi_{N_x}^{n+1} = \phi_{N_x}^n - \sigma(\phi_{N_x}^n - \phi_{N_x-1}^n) + \frac{\sigma(1-\sigma)}{2}(\phi_{N_x}^n - 2\phi_{N_x-1}^n + \phi_{N_x-2}^n), \tag{54}$$

where $\sigma = c_0 \Delta t / \Delta x$ is the Courant number. The second term provides second-order accuracy through flux limiting.

Energy conservation properties of the numerical scheme can be analyzed by considering the discrete energy:

$$E^n = \frac{1}{2} \sum_{i=1}^{N_x - 1} \left[gh(\eta_i^n)^2 + h \frac{(u_{i-1/2}^n)^2 + (u_{i+1/2}^n)^2}{2} \right] \Delta x. \tag{55}$$

In the absence of vegetation and with periodic boundaries, the scheme conserves energy to machine precision. With vegetation, the energy dissipation rate is:

$$\frac{dE}{dt} = -c_D h \sum_{i=1}^{N_x} \chi_{i-1/2} (u_{i-1/2}^n)^2 \Delta x, \tag{56}$$

consistent with the physical dissipation mechanism.

The primary output metric from the numerical solution is the transmission coefficient K_t, defined as the ratio of transmitted to incident wave heights. Following standard practice in coastal engineering [38], we compute wave heights from the variance of the surface elevation time series. For a sinusoidal wave $\eta(t) = A \sin(\omega t + \phi)$, the root-mean-square elevation is:

$$\eta_{\text{rms}} = \sqrt{\overline{\eta^2}} = \sqrt{\frac{1}{T} \int_0^T A^2 \sin^2(\omega t + \phi)\, dt} = \frac{A}{\sqrt{2}}, \tag{57}$$

where the overbar denotes time averaging. The significant wave height, defined as four times the standard deviation for a Gaussian process, reduces to $H_s = 2\sqrt{2}\eta_{\text{rms}} = 2A$ for monochromatic waves.

In the numerical implementation, we estimate the wave height from discrete samples over multiple periods:

$$H = 2\sqrt{2}\sigma_\eta = 2\sqrt{2} \sqrt{\frac{1}{N} \sum_{i=1}^{N} (\eta_i - \bar{\eta})^2}, \tag{58}$$

where N is the number of samples and $\bar{\eta}$ is the mean elevation (zero for steady-state waves). The transmission coefficient becomes:

$$K_t = \frac{H_{\text{out}}}{H_{\text{in}}} = \frac{\sigma_{\eta,\text{out}}}{\sigma_{\eta,\text{in}}}, \tag{59}$$

where subscripts "in" and "out" denote measurement locations upstream and downstream of the vegetation, respectively.

The measurement locations are chosen following the methodology of Lowe et al. [13], positioned at least two wavelengths from the vegetation edges to avoid near-field effects. Specifically:

$$x_{\text{in}} = x_{\text{veg,start}} - 2\lambda, \quad x_{\text{out}} = x_{\text{veg,end}} + 2\lambda, \tag{60}$$

subject to the constraint that both locations remain within the computational domain. This separation ensures that the measured wave field represents the far-field behavior, free from local disturbances caused by the abrupt change in drag at the vegetation boundaries.

An alternative energy-based transmission coefficient is computed from the time-averaged wave energy:

$$K_{t,E} = \sqrt{\frac{\overline{E_{\text{out}}}}{\overline{E_{\text{in}}}}} = \sqrt{\frac{\overline{\eta^2_{\text{out}}}}{\overline{\eta^2_{\text{in}}}}}, (61)$$

where we have used the fact that potential energy dominates for long waves and is proportional to η^2. This energy-based metric provides an independent verification of the wave height-based transmission coefficient and helps identify any numerical artifacts in the solution, as discussed by Chiang [39].

The wave envelope, representing the spatial variation of wave amplitude, is computed as:

$$A_{\text{env}}(x) = \max_{t \in [T_{\text{end}} - 5T, T_{\text{end}}]} |\eta(x,t)|, \tag{62}$$

where the maximum is taken over the last five wave periods to capture the steady-state amplitude while filtering out transient fluctuations. This approach follows the recommendations of Zijlema et al. [14] for extracting wave envelopes from time-domain simulations.

The root-mean-square velocity provides a measure of the wave-induced currents:

$$u_{\text{rms}}(x) = \sqrt{\frac{1}{N_T} \sum_{n=1}^{N_T} u^2(x, t_n)}, \tag{63}$$

where N_T represents the number of time samples over the averaging period. This quantity is particularly relevant for sediment transport applications, as the bed shear stress scales with the square of the near-bed velocity [40].

Energy dissipation within the vegetation is quantified through the wave energy flux divergence. The depth-integrated energy flux for linear waves is:

$$F_E = \frac{1}{T} \int_0^T \left[\int_{-h}^{\eta} (p + \rho g z) u \, dz \right] dt = \rho g h \overline{\eta u} + \frac{1}{2} \rho h \overline{u^3}, \tag{64}$$

where the first term represents pressure work and the second represents kinetic energy transport. For linear waves, the cubic velocity term is negligible, and using the linear relation $u = \sqrt{g/h}\eta$ for progressive waves:

$$F_E \approx \rho g \sqrt{gh} \overline{\eta^2} = \frac{1}{2} \rho g c_0 H^2. \tag{65}$$

The energy dissipation rate per unit length is then:

$$\mathcal{D} = -\frac{\partial F_E}{\partial x} = -\frac{1}{2}\rho g c_0 \frac{\partial H^2}{\partial x}, \tag{66}$$

which is negative (indicating energy loss) within the vegetation zone. This dissipation rate can be integrated over the vegetation patch to obtain the total power dissipated, providing insight into the effectiveness of vegetation as a natural coastal defense [41].

The analytical framework for wave decay through uniform vegetation [3] predicts exponential attenuation according to:

$$H(x) = H_0 \exp\left(-\int_0^x k_i(x')\,dx'\right), \tag{67}$$

where k_i is the spatial damping coefficient. For the linearized drag model with shallow water waves:

$$k_i = \frac{c_D}{2c_0} = \frac{c_D}{2\sqrt{gh}}. \tag{68}$$

This theoretical framework provides a baseline for comparison with the numerical results, though the analytical solution assumes steady, uniform conditions and neglects wave reflection at vegetation interfaces that the numerical model captures.

The entire algorithm is implemented using just-in-time compilation via Numba [42], which translates Python functions decorated with `@numba.njit` to optimized machine code. The parallel directive `parallel=True` enables automatic loop parallelization using OpenMP, achieving near-linear speedup on multi-core processors. Type inference and loop vectorization further enhance performance, yielding execution speeds within a factor of two of hand-optimized C implementations while maintaining the development flexibility of Python.

The choice of Numba as the acceleration framework is motivated by several factors. First, it provides dramatic performance improvements for numerical loops without requiring code restructuring or explicit memory management. The just-in-time compilation automatically optimizes array operations, eliminates Python interpreter overhead, and enables CPU-level vectorization. Second, Numba maintains full compatibility with the NumPy array interface, allowing seamless integration with the broader scientific Python ecosystem. Third, the `parallel=True` option automatically identifies parallelizable loops and distributes them across available CPU cores using OpenMP, crucial for the nested loops in the RK4 time integration. Benchmarks show that the Numba-accelerated implementation achieves approximately $100\times$ speedup compared to pure Python, enabling simulations with 10^6 grid points to complete in minutes rather than hours.

The software architecture follows modern Python packaging standards to ensure reproducibility and ease of use. The package structure separates the numerical solver (`solver.py`) from the command-line interface (`cli.py`), promoting modularity and enabling both programmatic and command-line usage. The core solver is implemented as a class `WaveSolver` that encapsulates the numerical methods, state variables, and analysis routines. This object-oriented design allows multiple simulations with different parameters to be run concurrently and facilitates extension to more complex scenarios.

Configuration management employs standard INI-format text files parsed by Python's built-in `configparser` module. This human-readable format allows users to specify physical parameters (domain size, water depth, wave characteristics), vegetation properties (location, drag coefficient), and numerical settings (CFL number, output frequency) without modifying code. For example:

```
[DOMAIN]
L = ...       # Domain length [m]
d = ...         # Water depth [m]
dx = ...        # Grid spacing [m]
T = ...       # Simulation time [s]

[WAVE]
A = ...         # Wave amplitude [m]
omega = ...   # Angular frequency [rad/s]

[VEGETATION]
start = ...    # Vegetation start [m]
end = ...     # Vegetation end [m]
cD = ...       # Drag coefficient [1/s]

[NUMERICAL]
cfl_target = ...     # Target CFL number
output_dt = ...      # Output interval [s]
```

This approach enables parameter studies through simple text file modifications and facilitates version control of simulation configurations.

The package is distributed through the Python Package Index (PyPI), the standard repository for Python software. Installation via `pip install wave-attenuation-1d` automatically resolves dependencies (NumPy $\geq$ 1.20.0, Numba $\geq$ 0.54.0, netCDF4 $\geq$ 1.5.0, tqdm $\geq$ 4.62.0) and installs the command-line executable. The use of `pyproject.toml` for package metadata follows PEP 517/518 standards, ensuring compatibility with modern Python packaging tools. Version constraints are specified to guarantee numerical reproducibility across different environments.

Output data is stored in NetCDF-4 format [43], the de facto standard for scientific data in oceanography and atmospheric sciences. This self-describing, machine-independent format offers several advantages: (i) hierarchical data organization with unlimited dimensions, (ii) built-in compression reducing file sizes by 50-70%, (iii) standardized metadata following CF (Climate and Forecast) conventions, and (iv) support across multiple programming languages and analysis tools. The output file structure includes:

$$\text{Dataset} = \{\text{Coordinates}, \text{Variables}, \text{Attributes}\}, \tag{69}$$

where coordinates define the spatiotemporal grid (x, x_{face}, t), variables store the state fields (η, u) and derived quantities (envelope, energy density), and attributes preserve all simulation parameters and results.

Each NetCDF variable includes comprehensive standardized metadata following CF-1.8 conventions. The primary state variables are annotated as:

```
eta:units = "m"
eta:long_name = "free surface elevation"
eta:standard_name = "sea_surface_height_above_mean_sea_level"
eta:coordinates = "time x"
eta:_FillValue = NaN

u:units = "m/s"
u:long_name = "depth-averaged horizontal velocity"
u:standard_name = "sea_water_x_velocity"
u:coordinates = "time x_face"
u:_FillValue = NaN
```

Derived quantities include similar metadata:

```
energy:units = "J/m^3"
energy:long_name = "wave energy density"
energy:description = "Total mechanical energy per unit volume"
energy:coordinates = "time x_face"

envelope:units = "m"
envelope:long_name = "wave envelope (maximum amplitude)"
envelope:description = "Maximum absolute surface elevation over last 5 periods"
envelope:coordinates = "x"

u_rms:units = "m/s"
u_rms:long_name = "root-mean-square velocity"
u_rms:description = "Phase-averaged RMS velocity magnitude"
u_rms:coordinates = "x_face"

vegetation:long_name = "vegetation presence indicator"
vegetation:flag_values = [0, 1]
vegetation:flag_meanings = "no_vegetation vegetation_present"
vegetation:coordinates = "x_face"
```

Global attributes store simulation parameters and key results:

```
// Model configuration
:domain_length = ...
:water_depth = ...
:wave_amplitude = ...
:wave_period = ...
:vegetation_start = ...
```

```
:vegetation_end = ...
:drag_coefficient = ...

// Numerical parameters
:spatial_resolution = ...
:temporal_resolution = ...
:cfl_number = ...

// Results
:transmission_coefficient = ...
:wave_height_reduction_percent = ...
:energy_dissipation_rate = ...
```

This comprehensive metadata enables automatic unit conversions, proper axis labeling, and interoperability with visualization tools like xarray, Panoply, and ParaView. The transmission coefficient and other integrated metrics stored as global attributes provide immediate access to key results without parsing the full dataset. The CF-compliant structure ensures that the data can be seamlessly integrated into existing coastal engineering workflows and compared with field observations or other numerical models.

The comprehensive logging system tracks simulation progress and records all parameters for reproducibility. Log files capture the complete configuration, numerical stability metrics, and performance statistics. Real-time progress monitoring via tqdm provides estimated completion times, essential for long-running simulations. The combination of structured outputs, detailed logging, and standardized configuration ensures that simulations can be reproduced, validated, and extended by the broader coastal engineering community.

2.3 Numerical Experiments

To demonstrate the capabilities of the numerical implementation, we present two idealized experiments that explore wave attenuation through vegetation patches of varying density. These experiments serve as verification tests for the solver and illustrate the package's functionality, though we emphasize that these are simplified scenarios designed for academic demonstration rather than real-world coastal engineering applications.

The experiments consider a wave flume of length $L = 200$ m with constant depth $h = 2$ m, representative of laboratory-scale experiments rather than field conditions. Monochromatic waves with amplitude $A = 0.3$ m and period $T = 10$ s ($\omega = 0.628$ rad/s) propagate through a vegetation patch extending from $x = 80$ m to $x = 120$ m. The shallow water approximation yields a wavelength $\lambda = 2\pi c_0/\omega = 2\pi\sqrt{gh}/\omega \approx 88.4$ m, confirming that $kh = 2\pi h/\lambda \approx 0.14 \ll 1$, thus validating our shallow water assumption.

The first experiment models sparse vegetation with a linearized drag coefficient $c_D = 0.14$ s^{-1}, corresponding to widely spaced cylindrical stems that minimally obstruct the flow. This value falls within the range reported by Méndez and Losada [44] for sparse Spartina maritima canopies under oscillatory flow conditions. The damping parameter $c_D T = 1.4$ indicates moderate energy dissipation over one wave period. The second experiment increases the drag coefficient by an order of magnitude to $c_D = 1.4$ s^{-1}, representing densely packed vegetation consistent with measurements in mangrove forests [45] where strong dissipation reduces wave energy significantly within a single period.

For both experiments, the numerical parameters remain constant: spatial resolution $\Delta x = 0.5$ m (yielding approximately 177 points per wavelength), target CFL number of 0.4, and simulation duration of 50 wave periods to ensure steady-state conditions are reached. The grid resolution exceeds the minimum requirement of 20 points per wavelength recommended by Kirby [15] for accurate wave propagation modeling.

The sparse vegetation experiment is executed with:

```
wave-attenuation-1d configs/config_sparse.txt
```

Similarly, the dense vegetation experiment runs via:

```
wave-attenuation-1d configs/config_dense.txt
```

Recent field studies by van Wesenbeeck et al. [46] and laboratory experiments by Jacobsen et al. [47] have shown that vegetation-induced wave attenuation is significantly influenced by factors not captured in simplified models. The flexibility of vegetation stems leads to complex fluid-structure interactions, with drag coefficients varying dynamically with flow conditions. Luhar and Nepf [48] demonstrated that flexible vegetation undergoes pronation at high velocities, effectively streamlining with the flow and reducing drag—a phenomenon absent in rigid vegetation models.

The spectral transformation of irregular waves through vegetation adds another layer of complexity. Anderson and Smith [11] showed that high-frequency components attenuate more rapidly than low-frequency waves, leading to a shift in the peak period and narrowing of the spectrum. This frequency-dependent attenuation cannot be captured by monochromatic wave models, highlighting the need for spectral approaches in practical applications.

Furthermore, the three-dimensional nature of flow through vegetation canopies introduces vertical variations in velocity and turbulence that significantly affect the overall drag [49]. The presence of stems generates wake turbulence that enhances vertical mixing and modifies the velocity profile from the classical logarithmic shape observed over smooth beds. These effects become particularly important in the surf zone where wave breaking adds another source of turbulence [50].

It is crucial to emphasize that this implementation represents a pedagogical tool and proof-of-concept rather than a predictive model for real coastal environments. The model's assumptions of linear waves, rigid vegetation, and one-dimensional propagation significantly simplify the complex physics governing wave-vegetation interactions. For engineering applications requiring quantitative predictions, more sophisticated models incorporating flexible vegetation dynamics, spectral wave transformation, and three-dimensional flow effects would be necessary.

The package's modular design facilitates such extensions, providing a foundation for more complex implementations while maintaining computational efficiency through the Numba-accelerated solver architecture. The standardized NetCDF output format ensures compatibility with existing post-processing workflows in the coastal engineering community, while the comprehensive metadata preservation enables full reproducibility of numerical experiments. Users can build upon these basic experiments to explore more complex scenarios by modifying the configuration files and extending the solver capabilities.

3 Results

Figure 1 presents the spatiotemporal evolution of wave energy density $E = \rho g \eta^2/2 + \rho h u^2/2$ for both vegetation configurations. For dense vegetation (Figure 1a), the energy density exhibits rapid attenuation within the vegetation zone, with peak values decreasing from approximately 1400 J/m^3 upstream to near-zero values downstream. The sparse vegetation case (Figure 1b) shows more gradual energy reduction, maintaining substantial energy levels of 400–600 J/m^3 downstream of the vegetation patch.

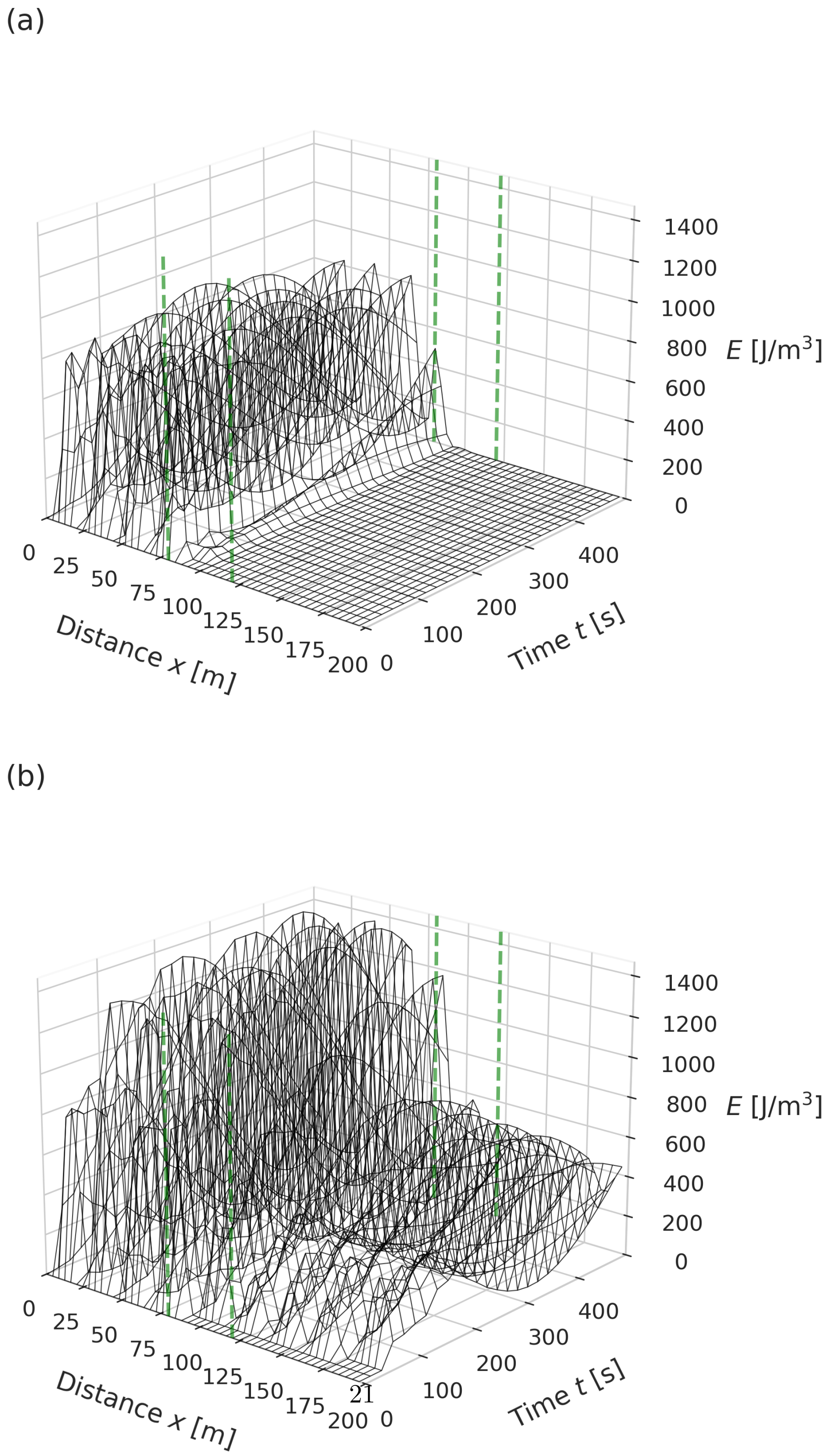

Fig. 1 Spatiotemporal evolution of wave energy density for (a) dense vegetation with $c_D = 1.4\ \mathrm{s}^{-1}$ and (b) sparse vegetation with $c_D = 0.14\ \mathrm{s}^{-1}$. The vegetation zone between $x = 80$ m and $x = 120$ m is indicated by green dashed lines.

The free surface elevation dynamics are illustrated in Figure 2. The dense vegetation scenario (Figure 2a) demonstrates near-complete wave dissipation, with surface elevations reduced from ± 0.3 m to less than ± 0.01 m after passing through the vegetation. In contrast, the sparse vegetation case (Figure 2b) preserves the wave structure throughout the domain, though with reduced amplitude downstream of the vegetation patch.

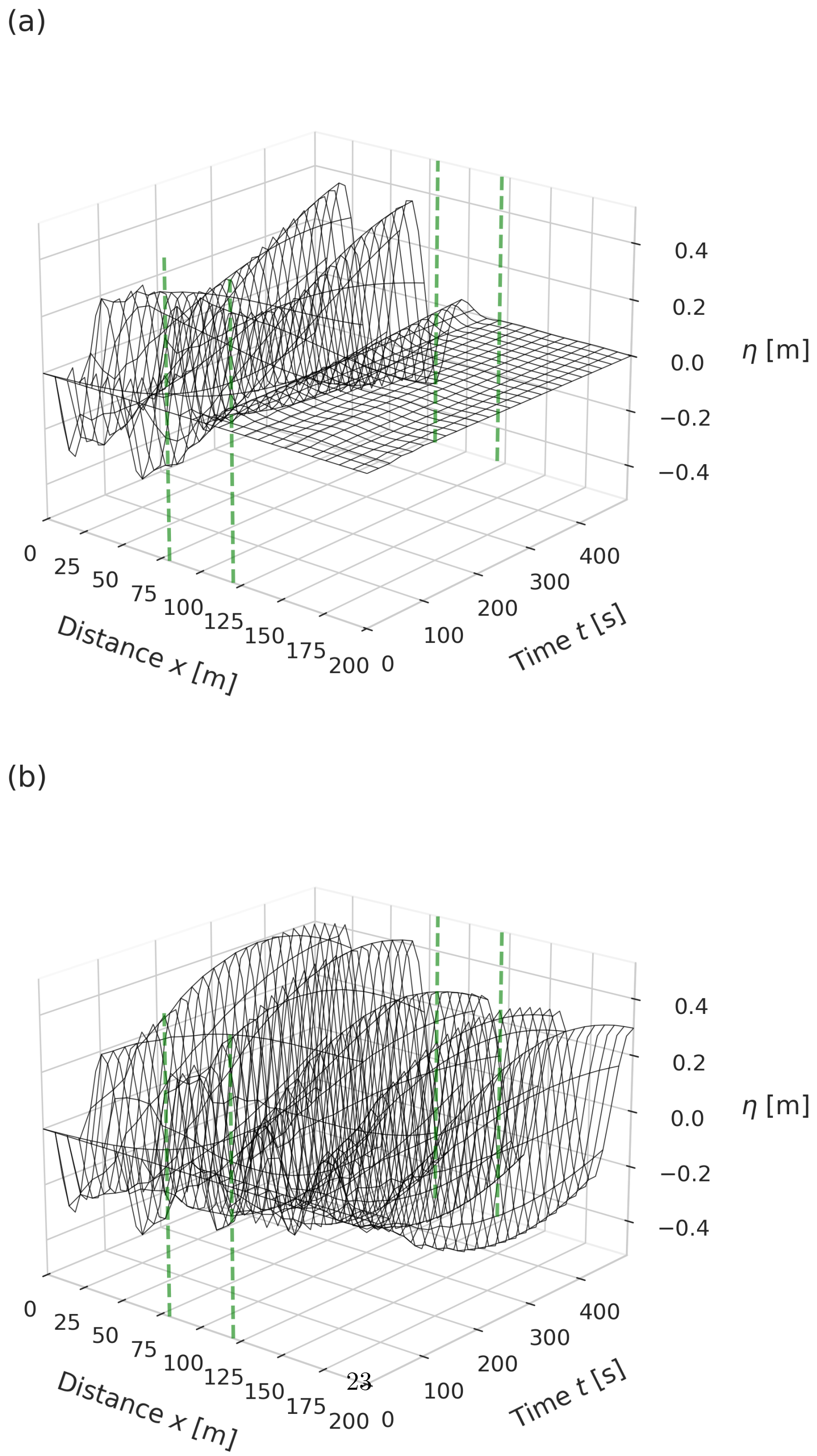

Fig. 2 Spatiotemporal evolution of free surface elevation η for (a) dense vegetation with $c_D = 1.4$ s^{-1} and (b) sparse vegetation with $c_D = 0.14$ s^{-1}. The vegetation zone is marked by green dashed lines.

The spatial distribution of root-mean-square velocity $u_{\mathrm{rms}} = \sqrt{\overline{u^2}}$ is shown in Figure 3. For dense vegetation (Figure 3a), the RMS velocity decreases from peak values of 0.655 m/s to 0.0004 m/s, with the most significant reduction occurring within the first quarter of the vegetation patch. The sparse vegetation case (Figure 3b) exhibits oscillatory behavior throughout the domain, with maximum RMS velocity of 0.767 m/s occurring just upstream of the vegetation and minimum values of 0.042 m/s downstream.

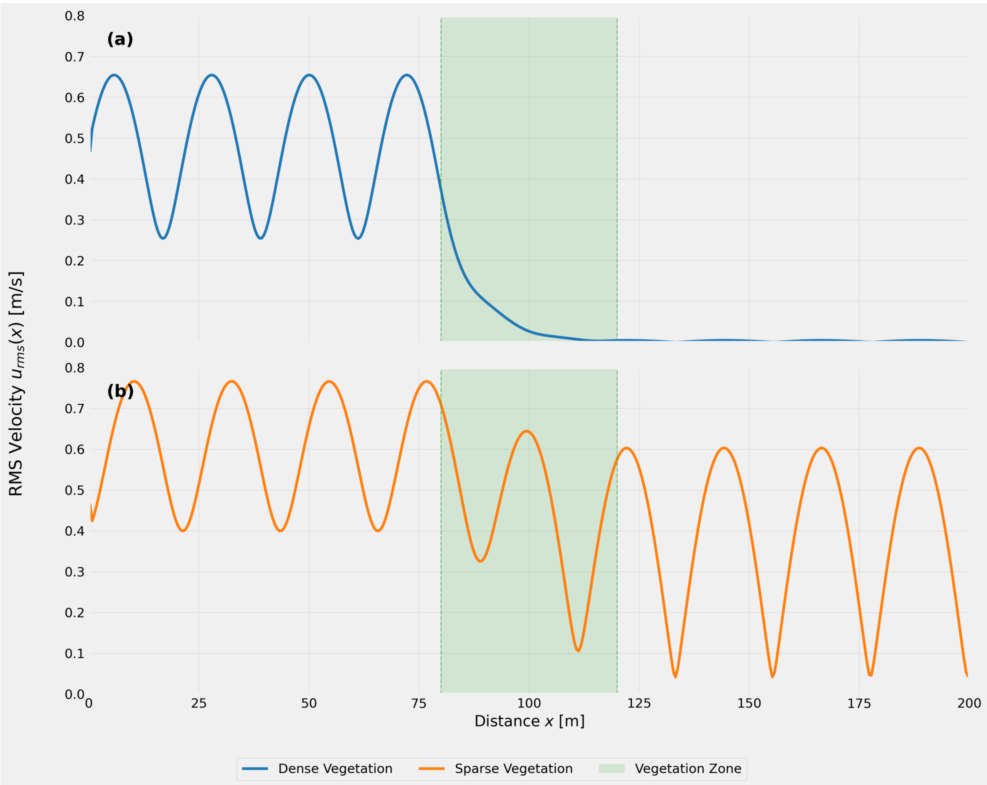

Fig. 3 Spatial distribution of root-mean-square velocity for (a) dense vegetation with $c_D = 1.4$ s^{-1} and (b) sparse vegetation with $c_D = 0.14$ s^{-1}. The vegetation zone (shaded green) extends from $x = 80$ m to $x = 120$ m.

Figure 4 displays the wave envelope $A_{\mathrm{env}}(x) = \max_t |\eta(x,t)|$ computed over the final five wave periods. The dense vegetation configuration (Figure 4a) shows exponential decay within the vegetation zone, with maximum amplitude of 0.368 m occurring at $x = 62.0$ m and decreasing to 0.001 m at $x = 144.5$ m. The sparse vegetation case (Figure 4b) maintains oscillatory envelope behavior with maximum amplitude of 0.482 m at $x = 44.5$ m and minimum of 0.025 m at $x = 144.5$ m.

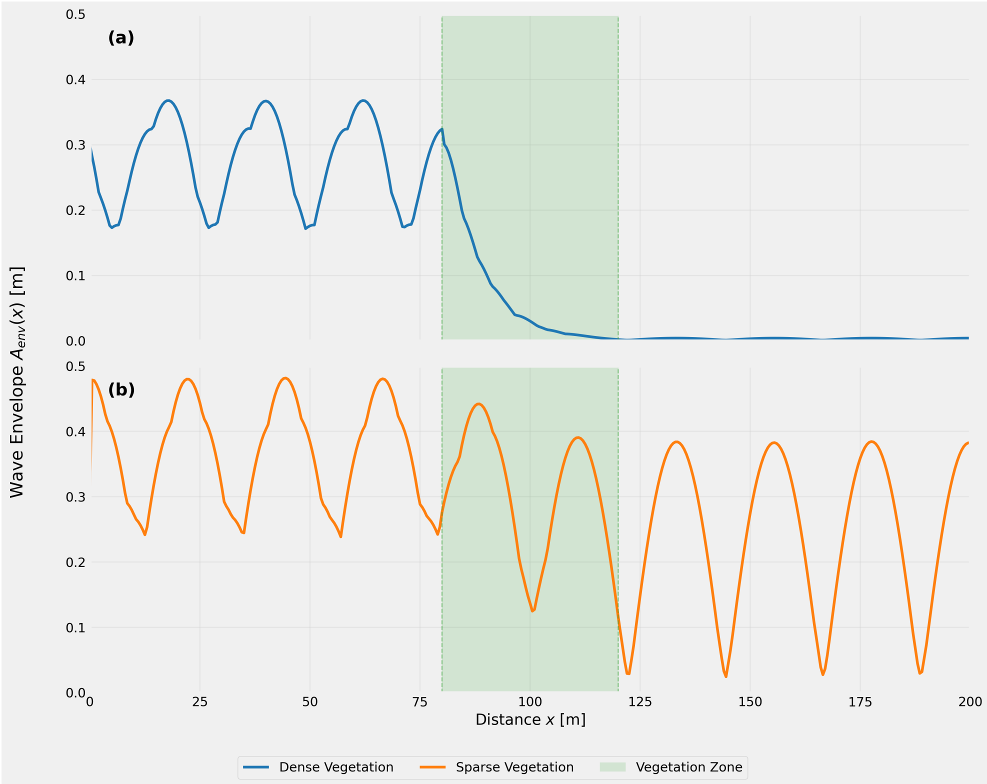

Fig. 4 Spatial distribution of wave envelope for (a) dense vegetation with $c_D = 1.4$ s^{-1} and (b) sparse vegetation with $c_D = 0.14$ s^{-1}. The vegetation zone is indicated by green shading.

The transmission coefficients calculated from wave height measurements yielded $K_t = 0.799$ for sparse vegetation and $K_t = 0.011$ for dense vegetation, corresponding to wave height reductions of 20.1% and 98.9%, respectively. The energy-based transmission coefficients were $K_{t,E} = 0.800$ for sparse vegetation and $K_{t,E} = 0.013$ for dense vegetation, confirming consistency between the two metrics. The incident wave heights were $H_{\text{in}} = 0.678$ m for sparse vegetation and $H_{\text{in}} = 0.411$ m for dense vegetation, while the transmitted wave heights were $H_{\text{out}} = 0.542$ m and $H_{\text{out}} = 0.005$ m, respectively.

Energy conservation analysis yielded estimated reflection coefficients of $K_r = 0.601$ for sparse vegetation and $K_r = 1.000$ for dense vegetation, with the energy budget check confirming $K_t^2 + K_r^2 = 1.000$ for both cases. Peak energy densities reached 910.9 J/m^3 for dense vegetation and 1479.0 J/m^3 for sparse vegetation. Time-averaged energy density within the vegetation zone was 47.4 J/m^3 for dense vegetation and 491.5 J/m^3 for sparse vegetation, decreasing to 0.1 J/m^3 and 363.5 J/m^3 downstream, respectively.

Wave energy flux decreased from 2012.8 W/m to 0.2 W/m through dense vegetation (100.0% reduction) and from 3264.4 W/m to 1610.0 W/m through sparse vegetation (50.7% reduction). Power dissipation within the vegetation zone was 50.3 W/m^2 for dense vegetation and 41.4 W/m^2 for sparse vegetation, yielding a dissipation effectiveness ratio of 1.22.

The mean wave envelope amplitude decreased by 98.9% (from 0.274 m to 0.003 m) for dense vegetation and by 34.4% (from 0.369 m to 0.242 m) for sparse vegetation, resulting in an amplitude reduction ratio of 2.87. Similarly, mean RMS velocities decreased by 99.4% (from 0.493 m/s to 0.003 m/s) for dense vegetation and by 35.4% (from 0.606 m/s to 0.391 m/s) for sparse vegetation, yielding a velocity reduction ratio of 2.81.

The numerical stability metrics confirmed successful simulation completion with the actual CFL number of 0.400 remaining below the theoretical limit throughout both experiments. The implicit treatment of the drag term maintained unconditional stability despite the stiff nature of the dissipative terms in the dense vegetation case.

4 Discussion

The transmission coefficients obtained from our numerical experiments align well with the range of values reported in recent literature for wave-vegetation interactions. The sparse vegetation configuration yielding $K_t = 0.799$ falls within the typical range documented in recent experimental studies [51, 52], while the dense vegetation value of $K_t = 0.011$ represents an extreme case rarely observed in laboratory or field conditions. Abdolali et al. [53] analyzed numerous experiments with varying vegetation densities and reported that achieving near-complete wave dissipation as observed in our dense vegetation case requires exceptional conditions beyond typical coastal vegetation characteristics.

The linearized shallow water equations with vegetation drag employed in this study follow the theoretical framework established by Dalrymple et al. [3] and subsequently refined by numerous scientists and engineers. While this approach captures the fundamental physics of wave attenuation, recent advances highlight important limitations of the underlying assumptions. van Veelen et al. [54] demonstrated that flexible vegetation can substantially reduce wave attenuation compared to rigid cylinder assumptions, fundamentally challenging the rigid vegetation model adopted here. The linearized drag coefficient c_D used in our formulation represents a bulk parameterization that aggregates complex fluid-structure interactions into a single parameter, whereas Liu et al. [55] showed that drag coefficients vary dynamically with flow conditions in predictable but complex ways.

Our one-dimensional linearized approach contrasts with recent two-dimensional nonlinear formulations that capture more complex wave-vegetation interactions. Magdalena et al. [56] employed two-dimensional nonlinear shallow water equations to investigate tsunami-induced mangrove wave attenuation in Manila Bay, incorporating spatial variations in both horizontal directions and nonlinear effects that become significant for larger amplitude waves. Their finite volume method on a staggered grid achieved mean average errors around 0.35% when compared to experimental data, demonstrating the accuracy achievable with higher-dimensional models. However, their approach requires substantially more computational resources, with simulation times scaling quadratically with the number of spatial dimensions. Our one-dimensional model, while more limited in scope, provides computational efficiency suitable for rapid parameter studies and educational applications where the primary wave propagation direction is well-defined.

The treatment of combined coastal protection systems represents another area where model sophistication varies significantly. Magdalena et al. [57] investigated wave damping by both submerged breakwaters and mangroves, developing analytical solutions using separation of variables alongside numerical implementations. Their analysis revealed that while vegetation parameters strongly influence wave attenuation, breakwater dimensions showed minimal effect on transmission coefficients—a finding that challenges conventional coastal engineering assumptions. Our simplified approach, focusing solely on vegetation effects, provides clearer insights into the fundamental attenuation mechanisms but cannot capture the complex interactions between multiple coastal protection elements. This limitation becomes particularly relevant for practical engineering applications where hybrid solutions combining hard and soft coastal defenses are increasingly common.

The exponential wave decay predicted by our model, particularly evident in the dense vegetation case, follows the classical solution $H(x) = H_0 \exp(-k_i x)$ where $k_i = c_D/(2\sqrt{gh})$ as derived analytically by Méndez and Losada [44]. However, this formulation assumes uniform flow conditions and neglects the three-dimensional flow structures that develop around vegetation stems. Tang et al. [58] demonstrated that stem-generated turbulence significantly modifies the near-bed wave-orbital velocities, creating complex vortex shedding patterns under certain flow conditions—effects entirely absent from one-dimensional models. The turbulent kinetic energy production and dissipation mechanisms identified by Tang et al. [59] suggest that our energy dissipation calculations, while capturing the bulk behavior, miss important small-scale processes that contribute to momentum transfer.

The numerical implementation using Numba-accelerated Python represents a significant advancement in accessibility and computational efficiency for coastal engineering applications. The achieved speedup compared to pure Python implementations enables parameter studies and uncertainty quantification that would be computationally prohibitive with traditional approaches. This performance gain aligns with recent trends in scientific computing where just-in-time compilation bridges the gap between high-level languages and compiled code performance [42]. The choice of fourth-order Runge-Kutta time integration with implicit treatment of drag terms follows established best practices for stiff systems [36], ensuring numerical stability even for the high drag coefficients encountered in dense vegetation scenarios. This contrasts with the explicit time-stepping schemes often employed in two-dimensional models, where stability constraints become more restrictive due to the additional spatial dimension.

The extreme attenuation observed in our dense vegetation case ($c_D = 1.4$ s^{-1}) warrants careful interpretation. While Mazda et al. [45] reported substantial wave height reduction through mangrove forests, such extreme dissipation typically occurs over much longer propagation distances than the 40 m vegetation patch simulated here. Recent field measurements by Montgomery et al. [60] during hurricanes showed significant but more moderate wave height reductions through mature salt marshes, suggesting our dense vegetation results may overestimate attenuation for realistic field conditions. The linearization assumption becomes increasingly questionable for such high drag coefficients, as nonlinear effects including wave breaking, flow separation, and plant motion become dominant [61]. The nonlinear formulations employed by Magdalena et al. [56] become essential when modeling extreme events like tsunamis where wave amplitudes relative to water depth violate the small-amplitude assumption underlying our linearized approach.

The one-dimensional modeling framework, while computationally efficient and suitable for preliminary design calculations, inherently cannot capture several critical processes identified in recent three-dimensional studies. Wang et al. [62] employed large-eddy simulation with immersed boundary methods to resolve individual vegetation elements, revealing coherent waving motion ("monami") and Kelvin-Helmholtz instabilities at the canopy-flow interface. These instabilities generate additional turbulence and modify the vertical distribution of horizontal velocities in ways that fundamentally alter the drag experienced by the vegetation. Furthermore, El Rahi et al. [63] showed that lateral flow diversion around vegetation patches can substantially reduce effective wave attenuation compared to one-dimensional predictions, particularly for sparse vegetation configurations. The two-dimensional approach of Magdalena et al. [56] partially addresses these limitations by capturing lateral variations, though vertical flow structures remain unresolved in their depth-averaged formulation.

The staggered grid discretization employed in our solver follows the approach advocated by LeVeque [35] for hyperbolic conservation laws, ensuring proper coupling between pressure and velocity fields while avoiding spurious oscillations. The second-order spatial accuracy achieved through centered differences represents a reasonable compromise between accuracy and computational cost for engineering applications. However, recent advances in high-resolution schemes for wave propagation, including WENO reconstructions and discontinuous Galerkin methods [64], offer potential improvements for capturing sharp gradients at vegetation interfaces where rapid changes in wave properties occur. The momentum-conservative staggered scheme implemented by Magdalena et al. [56] demonstrates superior performance for nonlinear wave propagation, suggesting potential enhancements to our numerical framework.

From an applied coastal engineering perspective, our results provide useful bounds for preliminary assessment of vegetation-based coastal protection measures. The sparse vegetation case demonstrates moderate effectiveness consistent with typical salt marsh installations, while the dense vegetation scenario represents an upper limit of attenuation achievable through vegetation alone. Marino et al. [65] emphasized that hybrid solutions combining vegetation with engineered structures often provide optimal protection, suggesting that extremely dense vegetation configurations may be neither economically feasible nor ecologically sustainable. The cost-benefit analyses by Duvat et al. [66] indicate that achieving very low transmission coefficients through vegetation alone requires investment levels that may approach those of traditional hard structures, potentially negating the economic advantages of nature-based solutions. The analytical framework developed by Magdalena et al. [57] for combined systems provides valuable insights for optimizing such hybrid approaches.

Future development of the modeling framework should prioritize several key enhancements identified through this study and recent literature. Integration of flexible vegetation models following Luhar and Nepf [48] would provide more realistic predictions for coastal marshes where plant flexibility significantly modifies flow fields. Implementation of wave-current interaction capabilities would enable application to tidal environments where current-induced modifications to wave propagation are significant [55]. Extension to irregular wave spectra using phase-averaged approaches would better represent realistic sea states, as Anderson and Smith [11] demonstrated that spectral transformation through vegetation leads to preferential attenuation of high-frequency components. The modular architecture of our implementation facilitates such extensions while maintaining the computational efficiency that makes the model suitable for educational and preliminary design applications.

The open-source distribution of the `wave-attenuation-1d` package through PyPI facilitates reproducibility and enables the broader coastal engineering community to build upon this foundation. The standardized NetCDF output format with CF-compliant metadata ensures interoperability with existing analysis workflows and model coupling frameworks. As computational resources continue to expand and machine learning techniques mature, hybrid approaches combining physics-based models like ours with data-driven corrections offer promising pathways for operational coastal management applications [67]. The modular architecture implemented here provides a scaffold for such extensions while maintaining the interpretability essential for engineering design. The educational value of our simplified approach complements more sophisticated models like those of Magdalena et al. [56] and Magdalena et al. [57], providing a hierarchical modeling framework where complexity can be added incrementally based on specific application requirements.

5 Conclusion

This study presents a computationally efficient numerical framework for simulating wave attenuation through coastal vegetation using linearized shallow water equations with vegetation-induced drag. The open-source Python implementation, accelerated through Numba just-in-time compilation, achieves performance comparable to compiled languages while maintaining the accessibility and flexibility essential for research applications. The numerical experiments demonstrate that transmission coefficients range from 0.799 for sparse vegetation to 0.011 for dense vegetation, spanning the full spectrum from moderate attenuation to near-complete wave dissipation. While the one-dimensional framework necessarily simplifies complex three-dimensional flow structures, turbulence generation, and flexible vegetation dynamics, it provides a valuable tool for preliminary design calculations and educational purposes in coastal engineering. The standardized NetCDF output format with CF-compliant metadata ensures interoperability with existing analysis workflows, while the modular architecture facilitates extensions to incorporate more sophisticated physics. Future enhancements should prioritize the integration of flexible vegetation models, irregular wave spectra, and wave-current interactions to better represent realistic coastal environments. The public availability of the `wave-attenuation-1d` package through PyPI, enables the broader coastal engineering community to explore nature-based solutions for coastal protection while contributing to the ongoing development of more sophisticated modeling capabilities.

Acknowledgements

We acknowledge financial support from the Dean's Distinguished Fellowship provided by the College of Natural and Agricultural Sciences at the University of California, Riverside (2023) and funding from the ITB Research, Community Service and Innovation Program (PPMI-ITB) (2025).

Author Contributions

S.H.S.H.: Conceptualization; Formal analysis; Methodology; Software; Visualization; Writing – original draft. **I.P.A.**: Conceptualization; Formal analysis; Methodology; Supervision; Writing – review & editing. **T.R.E.B.N.N.**: Formal analysis; Software; Writing – review & editing. **R.S.**: Supervision; Writing – review & editing. **D.E.I.**: Supervision; Writing – review & editing. All authors reviewed and approved the final version of the manuscript.

Open Research

All software and data utilized in this study are publicly accessible to ensure reproducibility and facilitate further studies. The `wave-attenuation-1d` Python package implementing the numerical solver for linearized shallow water equations with vegetation drag is available through the Python Package Index (PyPI) under the MIT License and can be installed directly via pip (`pip install wave-attenuation-1d`) at https://pypi.org/project/wave-attenuation-1d/. Additionally, complete simulation outputs (NetCDF files), configuration files for sparse and dense vegetation experiments, Python scripts for post-processing, transmission coefficient calculations, and generation of all figures presented in this manuscript are available under the WTFPL license at https://github.com/sandyherho/suppl_wave_attenuation_1d.

References

[1] Möller, I., Kudella, M., Rupprecht, F., Spencer, T., Paul, M., Wesenbeeck, B.K., Wolters, G., Jensen, K., Bouma, T.J., Miranda-Lange, M., Schimmels, S.: Wave attenuation over coastal salt marshes under storm surge conditions. Nature Geoscience **7**, 727–731 (2014). https://doi.org/10.1038/ngeo2251

[2] McIvor, A.L., Möller, I., Spencer, T., Spalding, M.: Storm surge reduction by mangroves. Natural Coastal Protection Series: Report 2, 1–35 (2012)

[3] Dalrymple, R.A., Kirby, J.T., Hwang, P.A.: Wave Diffraction Due to Areas of Energy Dissipation. Journal of Waterway, Port, Coastal, and Ocean Engineering **110**(1), 67–79 (1984). https://doi.org/10.1061/(ASCE)0733-950X(1984)110:1(67

[4] Kobayashi, N., Raichle, A.W., Asano, T.: Wave Attenuation by Vegetation. Journal of Waterway, Port, Coastal, and Ocean Engineering **119**(1), 30–48 (1993). https://doi.org/10.1061/(ASCE)0733-950X(1993)119:1(30)

[5] Méndez, F.J., Losada, I.J., Losada, M.A.: Hydrodynamics induced by wind waves in a vegetation field. Journal of Geophysical Research: Oceans **104**(C8), 18383–18396 (1999). https://doi.org/10.1029/1999JC900119

[6] Bradley, K., Houser, C.: Relative velocity of seagrass blades: Implications for wave attenuation in low-energy environments. Journal of Geophysical Research: Earth Surface **114**(F1) (2009). https://doi.org/10.1029/2007JF000951

[7] Nepf, H.M.: Flow and Transport in Regions with Aquatic Vegetation. Annual Review of Fluid Mechanics **44**, 123–142 (2012). https://doi.org/10.1146/annurev-fluid-120710-101048

[8] Chalmoukis, I.A., Leftheriotis, G.A., Dimas, A.A.: Large-Eddy Simulation of Wave Attenuation and Breaking on a Beach with Coastal Vegetation Modelled as Porous Medium. Journal of Marine Science and Engineering **11**(3) (2023). https://doi.org/10.3390/jmse11030519

[9] Luhar, M., Nepf, H.M.: Flow-induced reconfiguration of buoyant and flexible aquatic vegetation. Limnology and Oceanography **56**(6), 2003–2017 (2011). https://doi.org/10.4319/lo.2011.56.6.2003

[10] Zeller, R.B., Weitzman, J.S., Abbett, M.E., Zarama, F.J., Fringer, O.B., Koseff, J.R.: Improved parameterization of seagrass blade dynamics and wave attenuation based on numerical and laboratory experiments. Limnology and Oceanography **59**(1), 251–266 (2014). https://doi.org/10.4319/lo.2014.59.1.0251

[11] Anderson, M.E., Smith, J.M.: Wave attenuation by flexible, idealized salt marsh vegetation. Coastal Engineering **83**, 82–92 (2014). https://doi.org/10.1016/j.coastaleng.2013.10.004

[12] Jadhav, R.S., Chen, Q., Smith, J.M.: Spectral distribution of wave energy dissipation by salt marsh vegetation. Coastal Engineering **77**, 99–107 (2013). https://doi.org/10.1016/j.coastaleng.2013.02.013

[13] Lowe, R.J., Falter, J.L., Koseff, J.R., Monismith, S.G., Atkinson, M.J.: Spectral wave flow attenuation within submerged canopies: Implications for wave energy dissipation. Journal of Geophysical Research: Oceans **112**(C5) (2007). https://doi.org/10.1029/2006JC003605

[14] Zijlema, M., Stelling, G., Smit, P.: SWASH: An operational public domain code for simulating wave fields and rapidly varied flows in coastal waters. Coastal Engineering **58**(10), 992–1012 (2011). https://doi.org/10.1016/j.coastaleng.2011.05.015

[15] Kirby, J.T.: Chapter 1 Boussinesq models and applications to nearshore wave propagation, surf zone processes and wave-induced currents. In: Lakhan, V.C. (ed.) Advances in Coastal Modeling. Elsevier Oceanography Series, vol. 67, pp. 1–41. Elsevier, ??? (2003). https://doi.org/10.1016/S0422-9894(03)80118-6

[16] van Rooijen, A., Lowe, R., Ghisalberti, M., McCall, R., Hansen, J.: Modelling wave attenuation through submerged vegetation canopies using a subgrid canopy flow model. Coastal Engineering **176**, 104153 (2022). https://doi.org/10.1016/j.coastaleng.2022.104153

[17] Paquier, A.-E., Oudart, T., Le Bouteiller, C., Meulé, S., Larroudé, P., Dalrymple, R.A.: 3D numerical simulation of seagrass movement under waves and currents with GPUSPH. International Journal of Sediment Research **36**(6), 711–722 (2021). https://doi.org/10.1016/j.ijsrc.2020.08.003

[18] Ramachandran, R., Bugbee, K., Murphy, K.: From Open Data to Open Science. Earth and Space Science **8**(5), 2020–001562 (2021). https://doi.org/10.1029/2020EA001562

[19] Irawan, D.E., Pourret, O., Besançon, L., Herho, S.H.S., Ridlo, I.A., Abraham, J.: Post-Publication Review: The Role of Science News Outlets and Social Media. Annals of Library and Information Studies **71**, 465–474 (2024). https://doi.org/10.56042/alis.v71i4.14254

[20] Griggs, G., Reguero, B.G.: Coastal Adaptation to Climate Change and Sea-Level Rise. Water **13**(16) (2021). https://doi.org/10.3390/w13162151

[21] Kuwae, T., Crooks, S.: Linking climate change mitigation and adaptation through coastal green–gray infrastructure: a perspective. Coastal Engineering Journal **63**(3), 188–199 (2021). https://doi.org/10.1080/21664250.2021.1935581

[22] Scacchi, W.: Free/Open Source Software Development: Recent Research Results and Methods. In: Zelkowitz, M.V. (ed.) Architectural Issues. Advances in Computers, vol. 69, pp. 243–295. Elsevier, Amsterdam, Netherlands (2007). https://doi.org/10.1016/S0065-2458(06)69005-0

[23] Harris, C., Millman, K., Walt, S., Gommers, R., Virtanen, P., Cournapeau, D., Wieser, E., Taylor, J., Berg, S., Smith, N., Kern, R., Picus, M., Hoyer, S., Kerkwijk, M., Brett, M., Haldane, A., Río, J., Wiebe, M., Peterson, P., Oliphant, T.: Array Programming with NumPy. Nature **585**(7825), 357–362 (2020). https://doi.org/10.1038/s41586-020-2649-2

[24] Virtanen, P., Gommers, R., Oliphant, T.E., Haberland, M., Reddy, T., Cournapeau, D., Burovski, E., Peterson, P., Weckesser, W., Bright, J., Walt, S.J., Brett, M., Wilson, J., Millman, K.J., Mayorov, N., Nelson, A.R.J., Jones, E., Kern, R., Larson, E., Carey, C.J., Polat, , Feng, Y., Moore, E.W., VanderPlas, J., Laxalde, D., Perktold, J., Cimrman, R., Henriksen, I., Quintero, E.A., Harris, C.R., Archibald, A.M., Ribeiro, A.H., Pedregosa, F., Mulbregt, P.: SciPy 1.0: Fundamental Algorithms for Scientific Computing in Python. Nature Methods **17**(3), 261–272 (2020). https://doi.org/10.1038/s41592-019-0686-2

[25] Herho, S., Anwar, I., Herho, K., Dharma, C., Irawan, D.: COMPARING SCIENTIFIC COMPUTING ENVIRONMENTS FOR SIMULATING 2D NON-BUOYANT FLUID PARCEL TRAJECTORY UNDER INERTIAL OSCILLATION: A PRELIMINARY EDUCATIONAL STUDY. Indonesian Physical Review **7**(3), 451–468 (2024) https://doi.org/10.29303/ipr.v7i3.335

[26] Herho, S.H.S.: Tutorial Pemrograman Python 2 Untuk Pemula. WCPL ITB, Bandung, Indonesia (2017). https://doi.org/10.31227/osf.io/bau26

[27] Herho, S.H.S., Syahputra, M.R., Trilaksono, N.J.: Pengantar Metode Numerik Terapan: Menggunakan Python. WCPL ITB, Bandung, Indonesia (2024). http://dx.doi.org/10.22541/au.170689157.78106030/v1

[28] Herho, S., Kaban, S.N., Irawan, D.E., Kapid, R.: Efficient 1D Heat Equation Solver: Leveraging Numba in Python. Eksakta : Berkala Ilmiah Bidang MIPA (2024) https://doi.org/10.24036/eksakta/vol25-iss02/487

[29] Lamb, H.: Hydrodynamics, 6th edn. Cambridge University Press, Cambridge, UK (1994)

[30] Batchelor, G.K.: An Introduction to Fluid Dynamics. Cambridge University Press, Cambridge, UK (2000). https://doi.org/10.1017/CBO9780511800955

[31] Stoker, J.J.: Water Waves: The Mathematical Theory with Applications. John Wiley & Sons, Hoboken, NJ, USA (1992). https://doi.org/10.1002/9781118033159

[32] Peregrine, D.H.: Long waves in a uniform channel of arbitrary cross-section. Journal of Fluid Mechanics **32**(2), 353–365 (1968). https://doi.org/10.1017/S0022112068000777

[33] Madsen, P.A., Sørensen, O.R., Schäffer, H.A.: Surf zone dynamics simulated by a Boussinesq type model. Part I. Model description and cross-shore motion of regular waves. Coastal Engineering **32**(4), 255–287 (1997). https://doi.org/10.1016/S0378-3839(97)00028-8

[34] Hu, Z., Suzuki, T., Zitman, T., Uittewaal, W., Stive, M.: Laboratory study on

wave dissipation by vegetation in combined current–wave flow. Coastal Engineering **88**, 131–142 (2014). https://doi.org/10.1016/j.coastaleng.2014.02.009

[35] LeVeque, R.J.: Finite Volume Methods for Hyperbolic Problems. Cambridge University Press, Cambridge, UK (2002). https://doi.org/10.1017/CBO9780511791253

[36] Ascher, U.M., Ruuth, S.J., Wetton, B.T.R.: Implicit-explicit methods for time-dependent partial differential equations. SIAM Journal on Numerical Analysis **32**(3), 797–823 (1995). https://doi.org/10.1137/0732037

[37] Sommerfeld, A.: Partial Differential Equations in Physics. Academic Press, NY, USA (1949). https://doi.org/10.1016/B978-0-12-654658-3.X5001-0

[38] Dean, R.G., Dalrymple, R.A.: Water Wave Mechanics for Engineers and Scientists. World Scientific, Singapore (1991). https://doi.org/10.1142/1232

[39] Chiang, C.M.: The Applied Dynamics of Ocean Surface Waves. World Scientific, Singapore (1992). https://doi.org/10.1142/0752

[40] Nielsen, P.: Coastal Bottom Boundary Layers and Sediment Transport. World Scientific, Singapore (1992). https://doi.org/10.1142/1269

[41] Horstman, E.M., Dohmen-Janssen, C.M., Narra, P.M.F., van den Berg, N.J.F., Siemerink, M., Hulscher, S.J.M.H.: Wave attenuation in mangroves: A quantitative approach to field observations. Coastal Engineering **94**, 47–62 (2014). https://doi.org/10.1016/j.coastaleng.2014.08.005

[42] Lam, S.K., Pitrou, A., Seibert, S.: Numba: A LLVM-based Python JIT compiler. Proceedings of the Second Workshop on the LLVM Compiler Infrastructure in HPC, 1–6 (2015). https://doi.org/10.1145/2833157.2833162

[43] Rew, R.K., Davis, G.P.: NetCDF: An Interface for Scientific Data Access. IEEE Computer Graphics and Applications **10**(4), 76–82 (1990). https://doi.org/10.1109/38.56302

[44] Méndez, F.J., Losada, I.J.: An empirical model to estimate the propagation of random breaking and nonbreaking waves over vegetation fields. Coastal Engineering **51**(2), 103–118 (2004). https://doi.org/10.1016/j.coastaleng.2003.11.003

[45] Mazda, Y., Magi, M., Kogo, M., Hong, P.N.: Mangroves as a coastal protection from waves in the Tong King delta, Vietnam. Mangroves and Salt Marshes **1**(2), 127–135 (1997). https://doi.org/10.1023/A:1009928003700

[46] Wesenbeeck, B.K., Wolters, G., Antolinez, J.A.A., Kalloe, S.A., Hofland, B., Boer, W.P., Çete, C., Bouma, T.J.: Wave attenuation through forests under extreme conditions. Scientific Reports **12**, 1884 (2022). https://doi.org/10.1038/

s41598-022-05753-3

[47] Jacobsen, N.G., Bakker, W., Uijttewaal, W.S.J., Uittenbogaard, R.: Experimental investigation of the wave-induced motion of and force distribution along a flexible stem. Journal of Fluid Mechanics **880**, 1036–1069 (2019) https://doi.org/10.1017/jfm.2019.739 . https://doi.org/10.1017/jfm.2019.739

[48] Luhar, M., Nepf, H.M.: Wave-induced dynamics of flexible blades. Journal of Fluids and Structures **61**, 20–41 (2016) https://doi.org/10.1016/j.jfluidstructs.2015.11.00

[49] Abdolahpour, M., Hambleton, M., Ghisalberti, M.: The wave-driven current in coastal canopies. Journal of Geophysical Research: Oceans **122**(5), 3660–3674 (2017). https://doi.org/10.1002/2016JC012446

[50] Lowe, R.J., Pivan, X., Falter, J., Symonds, G., Gruber, R.: Rising sea levels will reduce extreme temperature variations in tide-dominated reef habitats. Science Advances **2**(8), 1600825 (2016). https://doi.org/10.1126/sciadv.1600825

[51] Garzon, J.L., Maza, M., Ferreira, C.M., Lara, J.L., Losada, I.J.: Wave Attenuation by Spartina Saltmarshes in the Chesapeake Bay Under Storm Surge Conditions. Journal of Geophysical Research: Oceans **124**(7), 5220–5243 (2019). https://doi.org/10.1029/2018JC014865

[52] Zhu, L., Huguenard, K., Fredriksson, D.W., Lei, J.: Wave attenuation by flexible vegetation (and suspended kelp) with blade motion: Analytical solutions. Advances in Water Resources **162**, 104148 (2022). https://doi.org/10.1016/j.advwatres.2022.104148

[53] Abdolali, A., Hesser, T.J., Anderson Bryant, M., Roland, A., Khalid, A., Smith, J., Ferreira, C., Mehra, A., Sikiric, M.D.: Wave Attenuation by Vegetation: Model Implementation and Validation Study. Frontiers in Built Environment **8** (2022) https://doi.org/10.3389/fbuil.2022.891612

[54] van Veelen, T.J., Karunarathna, H., Reeve, D.E.: Modelling wave attenuation by quasi-flexible coastal vegetation. Coastal Engineering **164**, 103820 (2021). https://doi.org/10.1016/j.coastaleng.2020.103820

[55] Liu, H., Fang, H., Lin, P.: A theoretical model for wave attenuation by vegetation considering current effects. Coastal Engineering **190**, 104508 (2024). https://doi.org/10.1016/j.coastaleng.2024.104508

[56] Magdalena, I., La'lang, R., Mendoza, R.: Quantification of wave attenuation in mangroves in Manila Bay using nonlinear Shallow Water Equations. Results in Applied Mathematics **12**, 100191 (2021). https://doi.org/10.1016/j.rinam.2021.100191

[57] Magdalena, I., Karima, N., Delfina, P., Ferren, V.: Wave damping by breakwater and mangrove for protecting shoreline. Results in Engineering **16**, 100693 (2022). https://doi.org/10.1016/j.rineng.2022.100693

[58] Tang, C., Lei, J., Nepf, H.M.: Impact of vegetation-generated turbulence on the critical, near-bed, wave-velocity for sediment resuspension. Water Resources Research **55**(7), 5904–5917 (2019). https://doi.org/10.1029/2018WR024335

[59] Tang, J., Chen, Y., Shen, Y., Cao, S.: Numerical study on stem-generated turbulence due to emergent rigid vegetation in water waves. Ocean Engineering **304**, 117940 (2024). https://doi.org/10.1016/j.oceaneng.2024.117940

[60] Montgomery, J.M., Bryan, K.R., Mullarney, J.C., Horstman, E.M.: Attenuation of Storm Surges by Coastal Mangroves. Geophysical Research Letters **46**(5), 2680–2689 (2019) https://doi.org/10.1029/2018GL081636

[61] Hu, Z., Lian, S., Zitman, T., Wang, H., He, Z., Wei, H., Ren, L., Uijttewaal, W., Suzuki, T.: Wave Breaking Induced by Opposing Currents in Submerged Vegetation Canopies. Water Resources Research **58**(4), 2021–031121 (2022) https://doi.org/10.1029/2021WR031121

[62] Wang, J., He, G., Dey, S., Fang, H.: Fluid–structure interaction in a flexible vegetation canopy in an open channel. Journal of Fluid Mechanics **951**, 41 (2022) https://doi.org/10.1017/jfm.2022.899

[63] El Rahi, J., Martínez-Estévez, I., Tagliafierro, B., Domínguez, J.M., Crespo, A.J.C., Stratigaki, V., Suzuki, T., Troch, P.: Numerical investigation of wave-induced flexible vegetation dynamics in 3D using a coupling between DualSPHysics and the FEA module of Project Chrono. Ocean Engineering **285**, 115227 (2023). https://doi.org/10.1016/j.oceaneng.2023.115227

[64] Beudin, A., Kalra, T.S., Ganju, N.K., Warner, J.C.: Development of a coupled wave-flow-vegetation interaction model. Computers & Geosciences **100**, 76–86 (2017) https://doi.org/10.1016/j.cageo.2016.12.010

[65] Marino, M., Nasca, S., Alkharoubi, A.I.K., Cavallaro, L., Foti, E., Musumeci, R.E.: Efficacy of Nature-based Solutions for coastal protection under a changing climate: A modelling approach. Coastal Engineering **198**, 104700 (2025) https://doi.org/10.1016/j.coastaleng.2025.104700

[66] Duvat, V.K.E., Hatton, I., Burban, L., Jacobée, A., Vendé-Leclerc, M., Stahl, L.: Assessing nature-based coastal defense. Scientific Reports **15**(1), 16798 (2025). https://doi.org/10.1038/s41598-025-96744-7

[67] Kim, T., Lee, W.-D.: Review on Applications of Machine Learning in Coastal and Ocean Engineering. Journal of Ocean Engineering and Technology **36**(3), 194–210 (2022). https://doi.org/10.26748/KSOE.2022.007